

Nitrogen-doped carbon skeleton loaded with PDI/MZO S-scheme photocatalyst with enhanced adsorption and photocatalysis activity

Yaru Wang, Xunxun Li, Wanjun Xu, Dongyun Chen^{*}, Najun Li, Qingfeng Xu, Hua Li, Jianmei Lu^{*}

College of Chemistry, Chemical Engineering and Materials Science, Collaborative Innovation Center of Suzhou Nano Science and Technology, Soochow University, Suzhou 215123, China



ARTICLE INFO

Keywords:
Adsorption-photocatalysis
Tetracycline
Organic-inorganic hybrid heterojunction
Ultra-high-performance

ABSTRACT

This report describes an organic-inorganic hybrid heterostructure comprising a nitrogen-doped carbon skeleton modified with perylene diimide and manganese-doped ZnO (NC@PDI/MZO). The high surface area of NC@PDI ($596.11\text{ m}^2\text{g}^{-1}$) significantly facilitated the tetracycline adsorption. Theoretical calculations reveal that NC@PDI/MZO has a maximum adsorption capacity of 224.72 mg/g of tetracycline under hydrogen bonding and $\pi\text{-}\pi$ interaction. The suitable band structures of PDI and MZO promoted efficient separation of photogenerated charge carriers and the formation of $\bullet\text{O}_2$ and $^1\text{O}_2$. The degradation rate of 50 mg/L tetracycline reached 99.9% after 40 min , and the degradation rate of 20 mg/L tetracycline reached 95.0% after only 10 min . In addition, due to the good match of adsorption rate and photocatalytic rate, NC@PDI/MZO has an unprecedented kinetic constant of 0.11 min^{-1} . This study provides insights that can guide the development of catalysts with well-matched adsorption and photocatalytic activity to remove contaminants from wastewater.

1. Introduction

With the rapid development of the global economy, humans face urgent challenges involving resource shortages and environmental contamination, where water shortage and pollution are the primary environmental problems [1–4]. Tetracycline (TC) is the second most commonly used antibiotic in the world. Nevertheless, it usually enters the human body through the food chain. Long-term intake of excessive TC-containing drinking water can trigger damage to the human liver, kidney, and other organs, as well as the nervous system, leading to drug-resistance [5–7]. Moreover, TC residues in aquatic systems can promote antibiotic-resistant bacteria and antibiotic-resistant genes, potentially leading to a major public health safety crisis. Thus, excessive dependence on and improper use of TC pose serious threats to human health and the ecological environment. It is therefore urgent to treat TC-containing effluent in a safe, green, and efficient manner to avoid a global environmental health crisis [8–12].

The main strategies for removing antibiotics from water include adsorption and photocatalytic degradation [13–15]. Meng et al. synthesized BM-S/ZVI@BC, and the maximum saturated adsorption capacity of BC/S/Fe⁰ for TC at 313 K reached 505.68 mg/g [16]. Yang

et al. prepared CoO@C as an adsorbent for effective TC removal, and it exhibited a maximum adsorption capacity of 769.43 mg/g [17]. The adsorption approach has the advantages of simple operation, low costs, and high efficiency; however, it is prone to the production of secondary pollutants [18,19]. Meanwhile, the photocatalytic approach has the advantages of environmental friendliness, good reproducibility, and economic efficiency [20,21]. Zhang et al. prepared a bismuth-rich photocatalyst (Bi₃O₄Br) to enhance molecular oxygen activation and the internal electric field, which increased the photocatalytic degradation and mineralization effects of TC [6]. Li et al. constructed Zr-S₄ active sites on ZnIn₂S₄ nanosheets, and their rate of photocatalytic degradation of TC was three times that of the original material, ZnIn₂S₄ [22]. However, photocatalysts generally have disadvantages of small specific surface areas and poor adsorption performance. Therefore, the combination of adsorption and photocatalysis technology represents a promising strategy for the removal of water pollutants.

To date, various synergistic adsorption-photocatalytic difunctional catalysts have been developed. Adsorption increases the contact between pollutants and photocatalysts, thereby improving the photocatalytic activity [23–26]. Adsorbents with excellent electrical conductivity can also facilitate the separation and transfer of

* Corresponding authors.

E-mail addresses: dychen@suda.edu.cn (D. Chen), lujm@suda.edu.cn (J. Lu).

light-induced carriers [13]. However, the photocatalytic rate of most catalysts does not match the adsorption rate, which leads to insufficient catalytic degradation rates of the pollutant. For example, Qiao et al. prepared magnetic graphene oxide/ZnO nanocomposite with a maximum adsorption capacity of 1590.28 mg/g [23]. Nevertheless, only 74% of the TC (50 mg/L) was degraded after 100 min of irradiation, corresponding to a reaction rate constant of 0.014 min^{-1} . Thin g-C₃N₄ nanosheets synthesized by Tian et al. attained TC adsorption equilibrium within 5 min, although the degradation rate of TC (20 mg/L) over 60 min only reached 75% [7]. Zou et al. used lignocellulose as the substrate of TiO₂ nanoparticles to prepare a composite aerogel for synergistic adsorption-photocatalytic removal of TC [26]. The catalyst showed strong adsorption of TC, with a maximum adsorption capacity of 70 mg/g; however, for 10 mg/L TC, only ~90% could be removed within 40 min. Because the photocatalytic reaction rate is not sufficiently fast, many of the adsorbed pollutants are concentrated on the surface of catalyst, which inhibits light absorption and the generation of active species. Although a catalyst may have excellent adsorption performance for pollutants, the photocatalytic performance of the adsorption-photocatalytic coordination system would hinder the overall activity [27–29]. Therefore, it is worthwhile to design and prepare bifunctional adsorption-photocatalytic catalysts with good matching between their adsorption and photocatalytic rates.

In this work, a nitrogen-doped carbon (NC) skeleton was modified with perylene diimide (PDI) via the amino group as a molecular link [30]. Subsequently, manganese-doped zinc oxide (MZO) was grown on the material in situ to promote TC removal from water through synergistic adsorption and photocatalysis (Scheme 1). N-doped carbon skeleton spheres have a large specific surface area and high porosity, which enables the enrichment of TC on the catalyst surface. Nitrogen doping can also improve the conductivity of the carrier. Meanwhile, the rich oxygen-containing functional groups and benzene rings of PDI support the adsorption of TC through hydrogen bonding and π - π interactions. Additionally, manganese doping effectively narrows the band gap of zinc oxide and facilitates the absorption of visible light. Mn-doped zinc oxide and PDI constitute an organic-inorganic hybrid heterojunction, which enables the effective separation of photogenerated carriers and ultra-high photocatalytic TC degradation efficiency. Overall, this study provides key insights that can be used to design and construct catalysts with well-matched adsorption and photocatalytic rates, which will be effective at eliminating contaminants from water.

2. Experimental section

2.1. Preparation of N-doped hollow porous carbon spheres

The mixture of 80 mL H₂O and 24 mL anhydrous ethanol was stirred at 1100 rpm for 5 min, then 1 mL ammonia and 1 mL TEOS were added, and 10 mL aqueous solution containing 0.5 g DA was added after stirring for 30 min. After stirring for 24 h, the product was fully washed with H₂O and ethanol and dried at 80 °C overnight. The resulting

product is named SiO₂@PDA. The dried solid powder was calcined in the nitrogen atmosphere at 800 °C for 120 min, and the heating rate was 5 °C/min. The resulting product is named SiO₂@NC. Weigh 300 mg of calcined black solid powder and add it into 50 mL HF (10 wt%) aqueous solution, stir at room temperature for 120 min, and wash with H₂O and ethanol three times each. After washing, the product was dried at 60 °C overnight to obtain nitrogen-doped hollow porous carbon spheres, named NC.

2.2. Preparation of NC@PDI

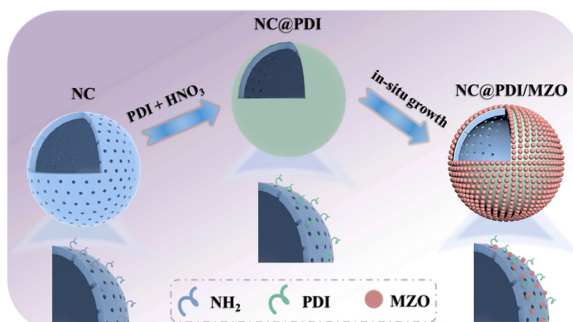
Ultrasonic dispersion of 18 mg perylene diimide into 90 mL H₂O, followed by the addition of 150 mg NC, stirring at room temperature for 60 min. 30 mL 4 M nitric acid aqueous solution was added into the above system and stirred at 60 °C for 90 min, then the product was washed to neutral and dried at 70 °C overnight to obtain PDI-coated N-doped hollow porous carbon spheres, named NC@PDI.

2.3. Preparation of NC@PDI/MZO

Disperse 50 mg NC@PDI into 50 mL ethanol, then add 0.75 mmol zinc acetate and 0.25 mmol manganese acetate, stirring continuously at 100 °C for 180 min, followed by ice bath to 0 °C. 5 mL ethanol solution containing 0.058 g LiOH was added to the system and stirred at 0 °C for 120 min. Then 25 mL H₂O was added into the system, stirring for another 15 min. The product was collected by centrifuge and dried at 60 °C overnight to obtain NC@PDI/MZO. The preparation of ZnO requires removing the addition of NC@PDI and manganese acetate and changing the amount of zinc acetate to 0.1 mmol. However, the preparation of MZO (manganese doped zinc oxide) requires the removal of NC@PDI. For the preparation of NC@PDI/1MZO and NC@PDI/3MZO, it is only necessary to halve and double the amounts of zinc acetate and manganese acetate, respectively, with the remaining steps unchanged.

2.4. Catalysts characterization

SEM (Scanning Electron Microscopy) and TEM (Transmission Electron Microscope) tests were operated to investigate the morphology and structure of catalysts by a Hitachi Regulus 8230 microscope and a HT7700 microscope, respectively. TEM high-resolution image, STEM image, and EDX (Energy Dispersive X-Ray Spectroscopy) energy spectrum analysis data was acquired on an FEI Tecnai F-20 microscope. The crystal information of the prepared samples was qualitatively analyzed by XRD (X-ray Powder Diffraction) technique performed on a D8 Advance X-ray diffractometer. With KBr as the white background, Fourier transform infrared spectroscopy (FT-IR) (VERTEX 70+HYPERION 2000) was performed to study the valence bonds and functional groups of the catalyst. The Si-2MP automatic specific surface area and porosity analyzer were employed to gain the specific surface area, pore size distribution, and pore volume dates using the Brunauer-Emmett-Teller (BET) and Barrett-Joyner-Halenda (BJH) methods. An Escalab 250Xi X-ray photoelectron spectrometer was exploited to achieve XPS (X-ray Photoelectron Spectroscopy) on the surface of the catalyst for the sake of analyzing the elemental species and chemical valence states, and their proportion. Ultraviolet-visible diffuse reflectance spectroscopy (UV-Vis DRS) of the catalyst was measured by UV-visible spectrophotometer (UV-3600). Photoluminescence (PL) spectra was recorded on a HITACHI F-4600 fluorescence spectrometer. ESR (Electron Spin Resonance) spectra analysis was carried out on a JES-X320 Electron spin resonance spectrometer. The zeta potential at different pH was measured on the Nano-ZS90 (Malvern Panalytical, British). An HPLC-MS system was employed to elucidate the photocatalytic performance of degradation intermediates.



Scheme 1. Schematic illustration of the synthesis of NC@PDI/MZO.

2.5. Adsorption experiments

In the adsorption experiment, 20 mg NC@P/2MZO was added to containing a certain concentration of TC solution (50 mL). At given time intervals, about 2 mL solution was sampled and filtered to remove the photocatalyst for the analysis of TC concentration by the dual-beam ultraviolet/visible spectrometer (Beijing Purkinje general instrument Co. Ltd, TU-1900). The TC adsorption capacity (q_t , mg/g) at time t (min) or equilibrium was evaluated by Eq. (1)

$$q_{t,e} = (C_0 - C_{t,e}) \cdot V/m \quad (1)$$

Where C_0 and $C_{t,e}$ (mg/L) is the TC concentration at initial and any time t or equilibrium, respectively; V (L) is the volume of the sample; m (g) is the amount of micelle.

2.6. Adsorption Isotherm Models

The Langmuir and Freundlich models were employed to fit the adsorption isotherms of NC@P/2MZO as described in Eqs. (2) and (3). The Langmuir adsorption model assumes that there is a constant adsorption energy with no interaction between adjacent adsorbates. The surface of the adsorbent is homogeneous, where the adsorption is restricted to a single layer with all of the sites possessing the same affinity for the target adsorbate. The Freundlich model is applied to multilayer adsorption. It assumes that adsorption occurs on the heterogeneous surface in which the adsorption heats and affinities are not uniformly distributed.

$$C_e/q_e = 1/(q_m k_L) + C_e/(q_m k_L) \quad (2)$$

$$\ln q_e = (1/n) \cdot \ln C_e + \ln k_F \quad (3)$$

where C_e is the equilibrium concentration of TC (mg/g); k_L (L/mg) and k_F (mg¹⁻ⁿ Lⁿ/g) is the Langmuir and Freundlich constant; q_m is the maximum adsorption capacity of NC@P/2MZO towards TC (mg/g), which could be defined as the monolayer saturation capacity; R_L is the separation factor, that is, $0 < R_L < 1$ for favorable adsorption, $R_L > 1$ for unfavorable adsorption, $R_L = 1$ for linear sorption and $R_L = 0$ for irreversible adsorption; n is an empirical parameter related to the adsorption "intensity", the adsorption is favorable when the values of $1/n$ between 0.1 and 1, and unfavorable when the $1/n$ exceeds 1.

Gibbs equations were conducted to calculate the adsorption thermodynamic parameters of ΔG as shown in Eq. (4)

$$\Delta G = -RT \ln k; k_d = C_e/q_e \quad (4)$$

Where T (K) is the reaction temperature (298 K), R (8.314 J/(mol•K)) is the gas constant, ΔG (kJ/mol) is Gibbs free energy, k is the adsorption equilibrium constant, which can be calculated by plotting $\ln k_d$ versus C_e and extrapolating C_e to zero, the value of the intercept is $\ln k$.

2.7. Adsorption Kinetic Models

The relationship between the TC adsorption and contact time were depicted using pseudo-first-order kinetic (PFO) mode and pseudo-second-order (PSO) kinetic model as shown in Eqs. (5) and (6)

$$\log(q_e - q_t) = -k_1 t + \log q_e \quad (5)$$

$$t/q_t = 1/k_2 q_e^2 + t/q_e \quad (6)$$

where q_t and q_e are the mass of TC adsorbed (mg/g) at any time t or equilibrium; k_1 and k_2 are the rate constants of the pseudo-first order (h^{-1}) and pseudo-second order (g/(mg•h)) kinetic process, respectively.

2.8. Photocatalytic activity measurement

The photocatalytic activities of as-prepared catalysts were measured

by photodegradation of TC using a 300 W xenon lamp (Perfect Light Technology Co., Ltd, China) with a 420 nm cut-off filter under the simulated solar light source, and the distance between the liquid surface and the lamp was always maintained at about 7 cm. When conducting the experiments, 20 mg photocatalyst was dispersed in an aqueous solution of TC (50 mL, 50 mg/L, pH = 5.5). Before irradiation, the systems were stirred in darkness for 30 min to achieve adsorption-desorption equilibrium. After that, the systems were exposed to visible light irradiation. The temperature of suspension was maintained at 25 °C in the circulating cooling water system during photocatalytic tests. At given time intervals, about 2 mL solution was sampled and filtered to remove the photocatalyst for the analysis of TC concentration by the dual-beam ultraviolet/visible spectrometer (Beijing Purkinje general instrument Co. Ltd, TU-1900). Finally, the concentration of TC was calculated by Eq. (7) ($\lambda_{\text{max}} = 356$ nm):

$$\text{Degradation efficiency} = (C_0 - C_t)/C_0 \times 100\% \quad (7)$$

At the same time, the kinetic curves of photocatalytic degradation of TC in different samples were obtained by pseudo-first-order kinetic model:

$$\ln(C_0/C_t) = kt \quad (8)$$

where k is the kinetic rate constant and t is the illumination time.

To investigate the effect of pH, the pH was controlled in the range of 3.5–11.5 by using a small amount of 0.1 M HCl and 0.1 M NaOH, and the initial TC concentration was 50 mg/L. Similarly, the effects of anion were studied by adding NaCl, NaNO₃, NaHCO₃ and Na₂SO₄ at concentrations of 5 mM, respectively. For the recyclability experiments, NC@P/2MZO was collected by centrifugation after reaction and dried in the oven at 60 °C for 12 h. The removal performance of recycled NC@P/2MZO was studied to investigate the reusability of catalyst.

2.9. Investigation of reactive species

In the quenching experiment, five different trapping agents (p-benzoquinone (P-BQ), isopropanol (IPA), ethylenediaminetetraacetic acid disodium salt (EDTA-2Na), silver nitrate (AgNO₃), β-carotene) (1 mM) were added into TC solution to detect the active species of photocatalytic reaction, respectively. P-BQ, IPA, EDTA-2Na, AgNO₃, β-carotene were used as trapping agents of superoxide radical ($\bullet\text{O}_2^-$), hydroxyl radical ($\bullet\text{OH}$), hole (h^+), electron (e^-), and singlet oxygen ($^1\text{O}_2$) in the TC degradation, respectively.

2.10. Photoelectrochemical experiment

The ultrasonic dispersion of the 5 mg photocatalyst with 5 mL water. The aforementioned solution was dropped onto 2 cm × 2 cm of prepared indium tin oxide (ITO) conductive glass, keep the 1 cm × 1 cm film area, and dry at 100 °C for 3 h. photocurrent (I-t), chemical impedance spectra (EIS), and Mott-Schottky were measured at an electrochemical workstation using a typical three-electrode electrolytic cell (CHI 660B, China). A conductive glass coated with photocatalyst was employed as the working electrode, a platinum sheet as the counter electrode and an Ag/AgCl electrode as the reference electrode in a 0.2 mol/L Na₂SO₄ solution test. Moreover, the test was carried out after the open circuit voltage had stabilized the system.

2.11. Density functional theory calculation

The density functional theory (DFT) calculations were performed using a Dmol3 module of Material Studio 2020. The generalized gradient approximation (GGA) method with Perdew-Burke-Ernzerhof (PBE) function was employed to describe the interactions between core and electrons. The force and energy convergence criterion were set

to 0.002 Ha Å⁻¹ and 10–5 Ha, respectively. When the optimization was completed, the ESP and mulliken charge calculations were performed.

3. Results and discussion

3.1. Morphological structural investigations

The morphologies and structures of the synthesized samples were characterized by scanning electron microscopy (SEM) and transmission electron microscopy (TEM), and the results are shown in Fig. 1, Fig. S1, and Fig. S2. After etching, NC becomes a hollow structure, with a wall thickness between 20 and 30 nm (Fig. 1a,d). Fig. 1b shows that the morphology of the sample did not change appreciably after coating with PDI, although Fig. 1e shows that the wall thickness of NC@PDI increased relative to that of NC. Compared with ZnO nanoparticles (Fig. S1c and Fig. S1f), MZO nanoparticles (Fig. S2a and Fig. S2d) are less prone to adhesion and agglomeration. After loading various amounts of MZO onto the NC@PDI surface via in situ growth, as shown in Fig. 1c,f and Fig. S2b,c,e,f, MZO was uniformly dispersed on

NC@PDI, indicating that a heterogeneous structure was formed. A high-resolution transmission electron microscopy (HR-TEM) image of the catalyst is shown in Fig. 1g. The lattice fringes are clearly observed with lattice spacings of 0.281, 0.237, and 0.162 nm, corresponding to the (100), (101), and (110) crystal faces of ZnO, respectively. Fig. 1h shows the high-angle annular dark-field scanning transmission electron microscopy (HAADF-STEM) images of NC@P/2MZO and the elemental maps for C, N, O, Zn, and Mn, respectively. The homogeneous distribution of C, N, O, Zn, and Mn elements over the entire surface of the catalyst confirmed the successful preparation of NC@P/2MZO.

The X-ray diffraction (XRD) images of NC and NC@PDI are shown in Fig. S3. Owing to the low content of PDI, only a wide peak at 26.5°, corresponding to the (002) crystal face of graphite, was observed in the XRD patterns of both samples. Fig. 2a presents the XRD patterns of ZnO, MZO, NC@P/1MZO, NC@P/2MZO, and NC@P/3MZO. Characteristic diffraction peaks of ZnO are observed in all samples, indexed as JCPDS card no.36–1451. The ZnO peaks at 31.8°, 34.4°, 36.3°, 47.5°, 56.6°, 62.9°, and 68.0° correspond to the (100), (002), (101), (102), (110), (103), and (112) crystal planes. Upon increasing the proportion of MZO,

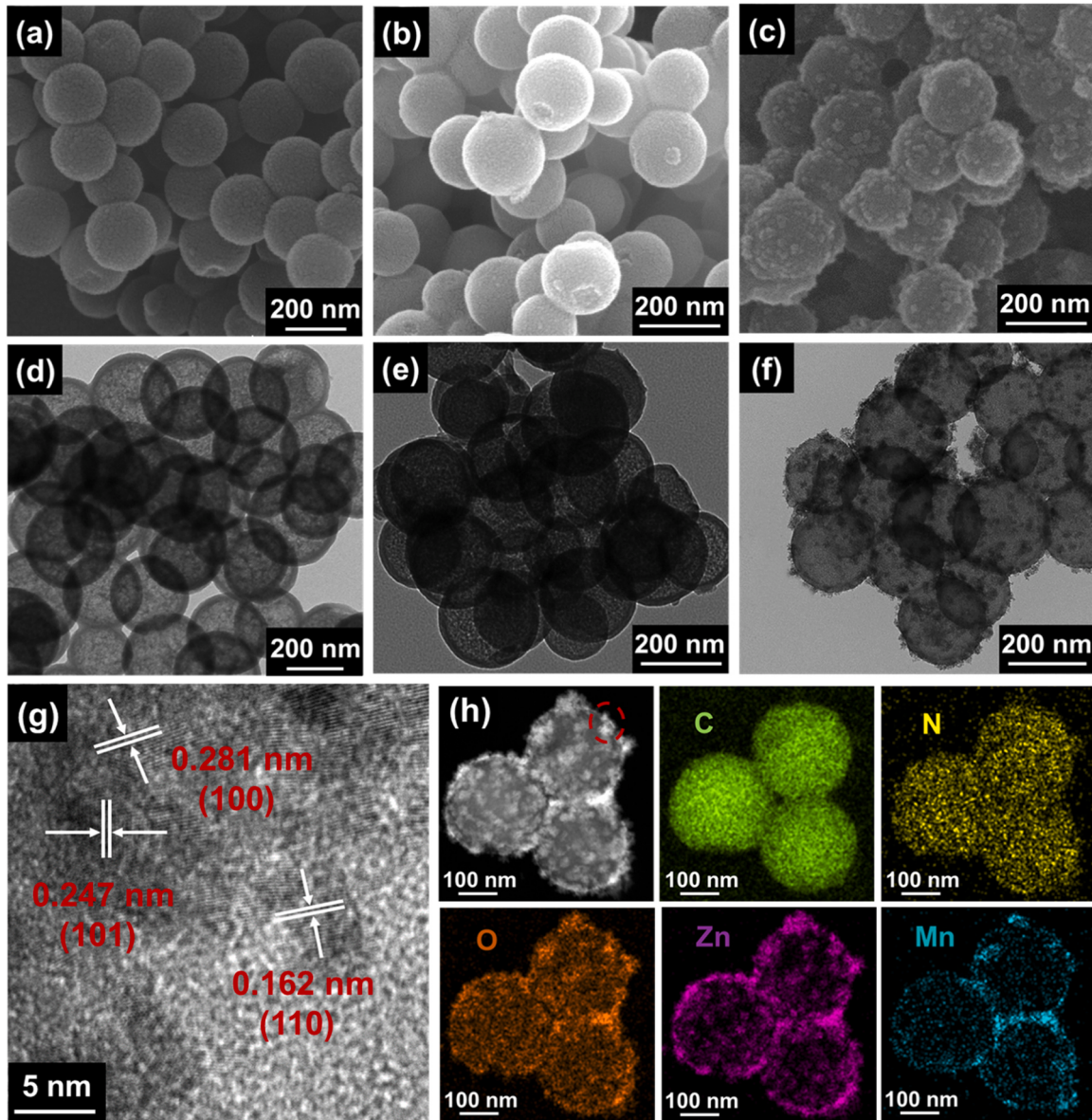


Fig. 1. SEM and TEM images of (a,d) NC, (b,e) NC@PDI, and (c,f) NC@P/2MZO, HR-TEM picture of NC@P/2MZO (g), HAADF-STEM image of NC@P/2MZO and STEM energy-dispersive X-ray spectroscopy elemental mappings of C, N, O, Zn and Mn (h).

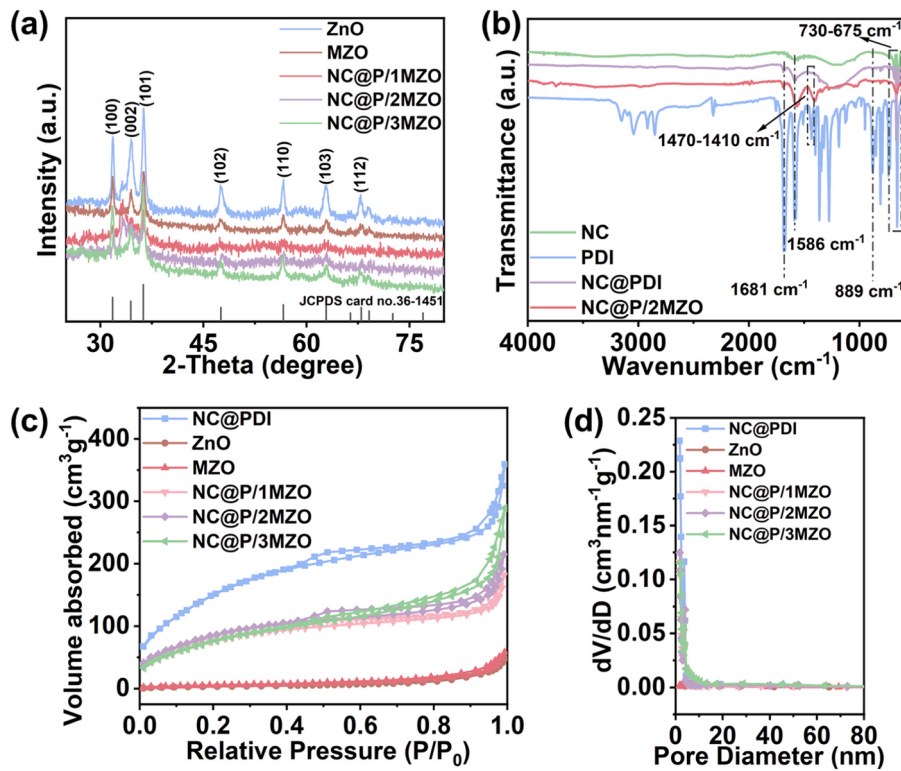


Fig. 2. (a) XRD patterns, (b) FT-IR spectra of the prepared catalysts, (c) N_2 -adsorption/desorption isotherms, and (d) pore size distributions of the prepared catalysts.

the intensity of the NC@PDI/MZO diffraction peak increased gradually. Fourier transform infrared spectrometry (FT-IR) was used to further characterize the composition of the samples, and the results are shown in Fig. 2b. The peak at $730\text{--}675\text{ cm}^{-1}$ was assigned to the $=\text{C}\text{--}\text{H}$ bending vibration; the peak at $1470\text{--}1410\text{ cm}^{-1}$ was attributed to the $\text{C}\text{--}\text{N}$ bending vibration; and the peak centered at 889 cm^{-1} represents the $\text{N}\text{--}\text{H}$ stretching vibration. In addition, the peaks at 1586 and 1681 cm^{-1} were attributed to the $\text{C}\text{=}\text{C}$ and $\text{C}\text{=}\text{O}$ stretching vibrations, respectively [30–33]. As expected, peaks related to PDI emerged after the NC surface was modified with PDI. When MZO was introduced to the NC@PDI material, the redshift of the peaks related to PDI indicated that a bond formed between PDI and MZO, which confirmed the successful preparation of the heterogeneous NC@P/MZO structure.

Nitrogen gas (N_2) adsorption-desorption isotherm experiments were carried out with the prepared catalysts, and the Brunauer-Emmett-Teller (BET) and Barrett-Joyner-Halenda (BJH) equations were used to calculate the specific surface area and pore size distribution. The results are presented in Fig. 2, Fig. S4, and Table S1. The N_2 adsorption-desorption isotherms of the prepared catalysts all had type IV characteristics (Fig. 2c and Fig. S4a) [34,35]. The pore size distribution in Fig. 2d and S4b and the pore size data in Table S1 also confirm that these materials have mesoporous structures. The specific surface area analysis (Table S1) revealed that NC had a large specific surface area ($628.73\text{ m}^2/\text{g}$). After incorporating PDI and loading MZO, the specific surface area was reduced slightly because the aperture was partially blocked. Nevertheless, the specific surface area of NC@P/2MZO reached $330.32\text{ m}^2/\text{g}$, which was 21.5 times that of ZnO. This large specific surface area is beneficial in terms of TC adsorption in water, and it also means that more active sites are exposed to promote the photocatalytic elimination of TC.

The surface elemental composition and valence states of the synthesized catalysts were characterized by X-ray photoelectron spectroscopy (XPS), and the results are presented in Fig. S5, and Fig. S6. The presence of each element could be easily observed in the survey data (Fig. S5a), thus demonstrating the successful preparation of the desired

catalysts. The high-resolution C 1s spectra of NC@PDI and NC@P/2MZO are shown in Fig. S5b, where the peak at 284.89 eV was assigned to $\text{C}\text{--}\text{C}/\text{C}\text{=}\text{C}$, and the peaks associated with $\text{C}\text{--}\text{O}$ and $\text{O}\text{--}\text{C}\text{=}\text{O}$ appeared at 286.19 and 290.00 eV , respectively [36]. The high-resolution N 1s spectra of NC@PDI and NC@P/2MZO were deconvoluted into four peaks (Fig. S5c): the peak associated with $\text{Py}\text{--}\text{N}$ was located at 398.43 eV , the peak associated with $\text{Pr}\text{--}\text{N}$ was located at 400.84 eV , the peak associated with $\text{G}\text{--}\text{N}$ was located at 403.13 eV , and the peak associated with $\text{O}\text{--}\text{N}$ was located at 406.13 eV [37]. The high-resolution O 1s spectra of ZnO and MZO could be deconvoluted into two peaks (Fig. S5d). The peak at 529.79 eV was attributed to $\text{Zn}\text{--}\text{O}$. Interestingly, this peak was shifted to higher binding energy after manganese doping. The peak at 531.65 eV was associated with $\text{H}\text{--}\text{O}$, which was attributed to the adsorbed water on the catalyst surface [38]. However, a $\text{C}\text{--}\text{O}$ -related peak at 533.38 eV appeared in the NC@P/2MZO spectrum, indicating that NC@PDI bonded to MZO. In the high-resolution $\text{Mn}\text{ 2p}_{3/2}$ spectra of MZO and NC@P/2MZO (Fig. S5e), the peaks at 641.17 and 642.98 eV were assigned to Mn^{2+} and Mn^{3+} , respectively [39]. The $\text{Zn}\text{ 2p}$ spectra of ZnO, MZO, and NC@P/2MZO (Fig. S5f) were deconvoluted into two peaks at 1021.44 and 1044.40 eV , which corresponded to $\text{Zn}\text{ 2p}_{3/2}$ and $\text{Zn}\text{ 2p}_{1/2}$, respectively [40]. After MZO was loaded onto NC@PDI, the characteristic peaks associated with carbonaceous species all shifted toward lower binding energy, whereas those associated with oxygen, manganese, and zinc species shifted toward higher binding energy. The same phenomenon was also observed for NC@P/1MZO and NC@P/3MZO (Fig. S6). This result indicates that the interactions between NC@PDI and MZO lead to the transfer of electrons from MZO to NC@PDI.

3.2. Optical and photoelectrochemical properties

The optical absorption properties of the series of photocatalysts were investigated by UV-vis diffuse reflection spectroscopy (UV-vis DRS), and the results are shown in Fig. 3a. The absorption edge of ZnO appeared at 409 nm , whereas the absorption edge of MZO was clearly

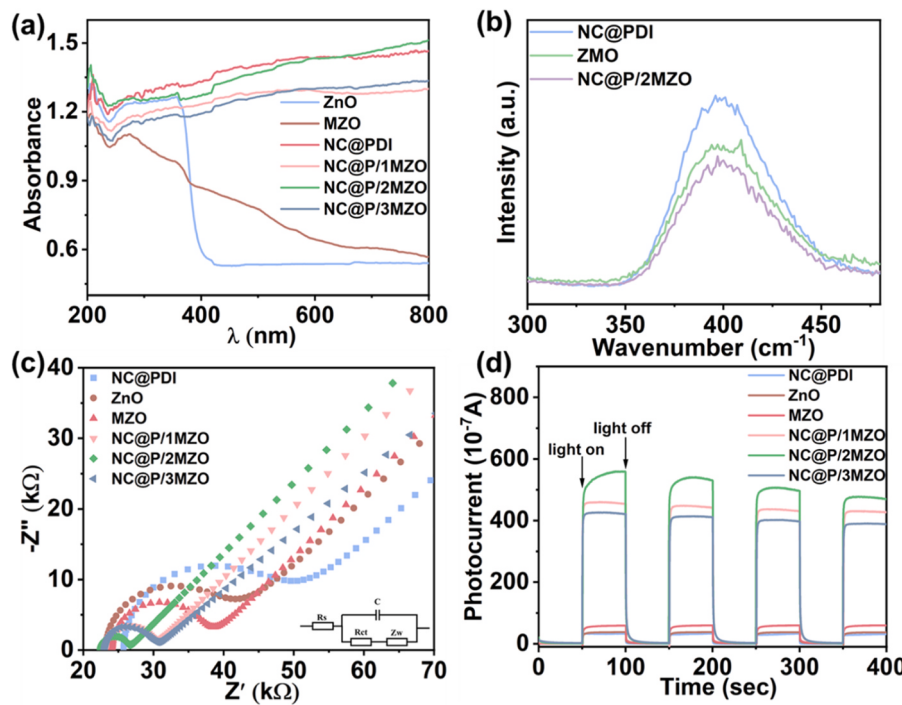


Fig. 3. (a) UV-vis DRS spectra, (b) steady-state PL spectra, (c) EIS Nyquist plots (inset: equivalent circuit diagram), and (d) transient photocurrent responses of as-prepared catalysts.

redshifted, which confirmed that manganese doping was beneficial to promote the absorption of visible light. The NC@PDI, NC@P/1MZO, NC@P/2MZO, and NC@P/3MZO catalysts exhibited strong light absorption over the entire visible range owing to the black NC carrier. Fig. 3b shows the steady-state photoluminescence (PL) spectra of catalysts. NC@PDI had a strong PL emission peak at 400 nm, while the PL intensity of NC@P/2MZO was much lower than that of NC@PDI and MZO, indicating a rapid spatial separation rate of photon-generated carriers. As shown in Fig. 3c, the arc radii of the composites were much smaller than those of NC@PDI and MZO, which confirmed that the coupling between NC@PDI and MZO effectively reduced the interfacial charge transfer resistance. Over the course of four on-off light cycles, NC@P/2MZO exhibited the strongest photocurrent density, which was approximately 15.6 times that of ZnO (Fig. 3d). Taken together, these results confirm that effective separation and rapid transfer of photo-generated electrons and holes can be achieved by the successful construction of an electric field at the interface of MZO and PDI. This system promotes the photocatalytic degradation of TC by NC@PDI/MZO.

The band structure of the catalyst can be determined using XPS valence band spectra and Mott-Schottky curves, and the results are shown in Fig. S7. The Evb-XPS of MZO and PDI are 2.54 and 1.00 eV (vs. NHE), respectively (Fig. S7a,b). The following conversion formula was used: $\text{EVB-NHE} = \text{EVB-XPS} + \varphi - 4.44$, where φ is the work function of the instrument (4.6 eV) [41]. The calculated valence bands (VB) for MZO and PDI were 2.70 and 1.16 eV, respectively. As shown in Fig. S7c,d, the positive tangent slopes of the MZO and PDI Mott-Schottky curves indicate that they are both n-type semiconductor materials, and the corresponding flat-band potentials are -0.46 and -0.67 eV (vs. Ag/AgCl, pH = 7). Accordingly, the conduction potentials are -0.26 and -0.47 eV, respectively (vs. NHE). Thus, MZO and PDI have staggered band structures, which are favorable for light-induced carrier separation and migration. Using the equation, $Eg = \text{EVB} - \text{ECB}$, the calculated bandgap values (Eg) of MZO and PDI are 2.96 and 1.63 eV, respectively. In addition, the Kubelka-Munk function was used to calculate the band gap of ZnO (3.11 eV; Fig. S8), which confirmed that doping with manganese ions effectively decreased the band gap of ZnO [42–44]. Considering that MZO and PDI have narrow band gaps, they are more

easily excited by visible light.

3.3. Exploration of adsorption properties

The adsorption kinetics, isotherms, and adsorption mechanism of NC@P/2MZO were investigated in detail. Adsorption isotherms are used to describe the dynamic equilibrium between adsorbent and adsorbate. At 298 K, the Langmuir (Eq. (2)) and Freundlich (Eq. (3)) isotherm models were used to fit the adsorption equilibrium data and investigate the adsorption mechanism; the results are shown in Fig. 4a,b and Table S2 [45]. The experimental data are more consistent with the Freundlich model (Fig. 4b), which indicated that the functional groups on NC@P/2MZO were uniformly distributed, and the TC adsorption process involved single-layer adsorption on the surface of NC@P/2MZO. Moreover, the maximum adsorption capacity at 298 K was determined to be 224.72 mg/g (Table S2), which confirmed that NC@P/2MZO has excellent adsorption potential for TC. Additionally, the separation factor $0.018 \leq R_L \leq 0.071$ and $n = 4.804 > 1$, which indicated favorable adsorption conditions. The Gibbs free energy $\Delta G = -11.030 \text{ kJ/mol}$ confirmed a thermodynamically spontaneous adsorption process. Pseudo-first-order (PFO) (Eq. (5)) and pseudo-second-order (PSO) (Eq. (6)) kinetic models were used to simulate the TC adsorption kinetics of NC@P/2MZO. The results show that the adsorption data fit well to both the PFO (Fig. 4c) and PSO models (Fig. 4d), although the correlation coefficient (R^2) of the PSO equation was closer to 1 (Table S2) [46,47].

To determine the adsorption force between TC and NC@P/2MZO, the NC@P/2MZO was analyzed before and after TC adsorption by FT-IR and XPS. After TC adsorption, the FT-IR spectrum of TC-NC@P/2MZO shows a TC peak in the range of 1600–750 cm^{-1} (Fig. S10), indicating that TC molecules were adsorbed on the surface of NC@P/2MZO. In addition, the peak corresponding to $\text{C}=\text{C}$ shifted from 1586 to 1564 cm^{-1} , which suggested that π - π interactions occurred between NC@P/2MZO and TC. The $\text{C}=\text{O}$ peak shifted from 1681 to 1674 cm^{-1} , likely due to the formation of hydrogen bonds. As shown in Fig. S10, after TC adsorption, the carbonaceous species shifted toward higher binding energy because of the π - π interactions. The formation of hydrogen bonds resulted in an average electron cloud density, which

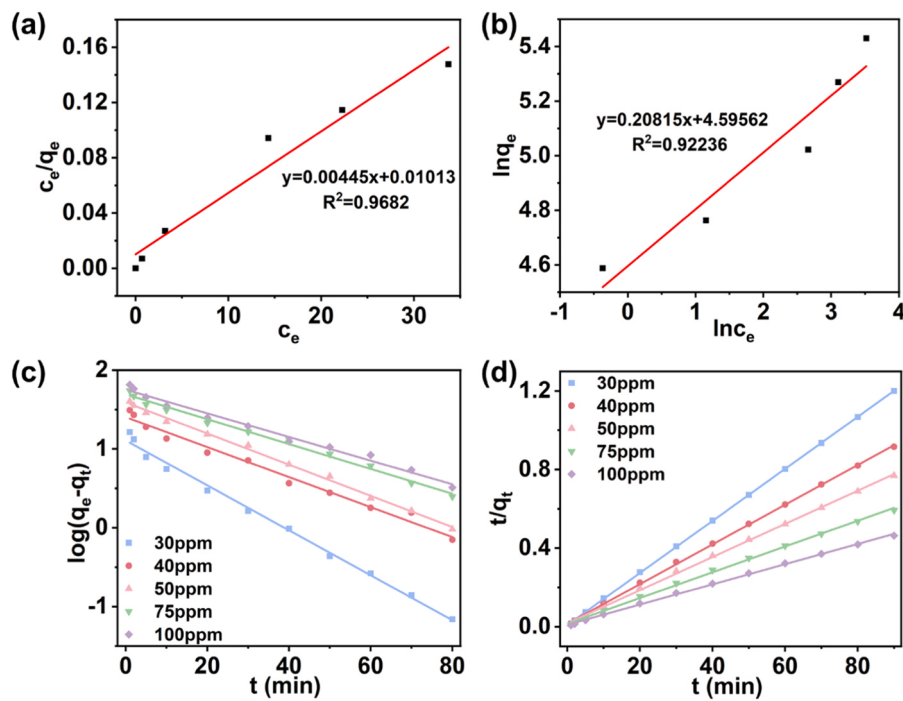


Fig. 4. (a,b) Adsorption isotherms of NC@P/2MZO for TC at 298 K and (c,d) adsorption kinetics of NC@P/2MZO for TC at various concentrations.

caused the oxygen- and nitrogen-containing species to shift toward lower binding energies. Acidic conditions were found to be more favorable for TC adsorption during photocatalytic tests (Fig. S19c), and therefore, we evaluated the Zeta potential of NC@P/2MZO at various pH values. As shown in Fig. S12a, the Zeta potential of NC@P/2MZO was positive in the pH range from 3.5 to 11.5; thus, the electrostatic interactions between NC@P/2MZO and TC molecules were excluded from the analysis. The stronger TC adsorption by NC@P/2MZO under acidic conditions could be attributed to the strong hydrogen bond interactions between the carbonyl and amino groups.

Density functional theory (DFT) was used to calculate and model the adsorption energy of π - π interactions and hydrogen bonds on TC (Fig. 5). Fig. 5a shows the hydrogen bond interactions of TC, corresponding to an adsorption energy of -140.0 kJ/mol. Fig. 5b depicts TC adsorption via π - π interactions, and the corresponding adsorption energy is -61.5 kJ/mol. Fig. 5c shows the details of the interactions between NC@P/2MZO and TC, which involved both π - π interactions and hydrogen bonds, with a total adsorption energy of -211.2 kJ/mol [48,49]. In addition, NC@P/2MZO has interesting adsorption properties for toluene, ethanol, and methanol at 300 mg/L (Fig. S12b), which suggested joint action of

different adsorption sites in the TC adsorption process. Based on the above analysis, it is reasonable to infer that the large surface area of NC@P/2MZO and the π - π and hydrogen bond interactions between NC@P/2MZO and TC molecules promote the adsorption of TC. Notably, TC adsorption on the catalyst surface impacted the electron transfer process. Carbonaceous species shifted toward higher binding energies, while oxygen, manganese, and zinc species shifted toward lower binding energies. This phenomenon confirmed that an internal electric field from PDI to MZO was formed at the interface between MZO and PDI.

3.4. Photocatalytic performance investigations

In this study, TC was selected as the target pollutant to evaluate the functionality of the NC@PDI/MZO heterostructure. The photocatalytic performance of NC@PDI is presented in Fig. S14. After five cycles, the TC removal rate could only be maintained at approximately 50%. NC@PDI reaching adsorption saturation was collected and placed into fresh 50 mg/L TC, and the TC degradation rate was still less than 30% over 60 min of light irradiation. Thus, NC@PDI exhibited excellent adsorption properties for TC, but the mismatch between the

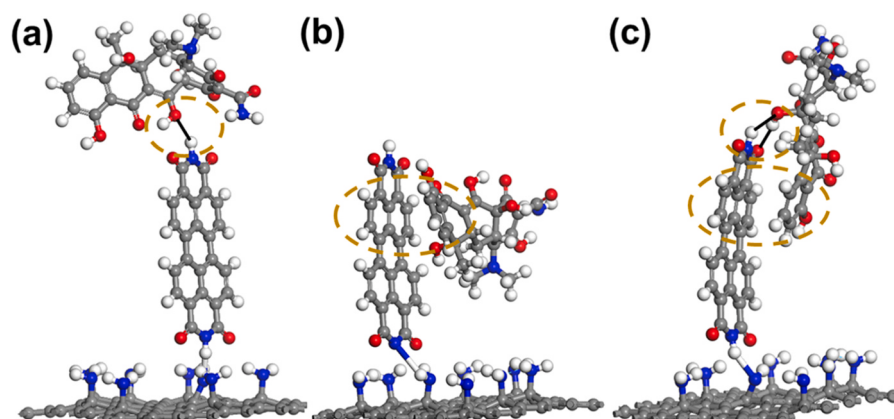


Fig. 5. Adsorption models: (a) hydrogen bond adsorption, (b) π - π adsorption, (c) π - π interactions and hydrogen bonds (co-adsorption).

photocatalytic rate and the adsorption rate led to unsatisfactory photocatalytic performance. The photocatalytic degradation performances with 50 mg/L TC for other prepared catalysts are shown in Fig. 6a. In the absence of a catalyst, TC did not self-degrade under visible light irradiation. Before the photocatalytic reaction, the adsorption-desorption equilibrium was achieved by stirring for 30 min under dark conditions. The TC adsorption rate of NC@P/2MZO reached 80% after 30 min in the dark; this activity was attributed to the large specific surface area of NC@P/2MZO and the hydrogen bond and π - π interactions between PDI and TC. The NC@P/2MZO catalyst showed the best TC degradation performance, reaching a 90% degradation rate for TC after 20 min of irradiation and a 99.9% degradation rate after 40 min irradiation. In addition, NC@P/2MZO photocatalytic degradation of 50 mg/L TC solution was tested for organic carbon content and the result was shown in Fig. S15. After 60 minutes of illumination, the total organic carbon content in the solution was 3.1 mg/L and the mineralization rate was 94%. Combined with the LC-MS/MS results (Fig. S20), it was confirmed that TC was degraded into small molecules such as carbon dioxide and water. This catalytic performance was far superior to that of a recently reported photocatalyst for TC degradation in terms of catalyst dosage and TC concentration (Table S3). In view of that the performance of the catalyst largely depends on the optical parameters of the catalyst, the optical thickness of the reactor and the total photon absorption rate [50–52], we formulated five catalysts in different concentrations and evaluated their photocatalytic TC degradation performance, as shown in Fig. S16. The best dosage of ZnO, MZO, NC@P/1MZO is 0.4 mg/mL, and the best dosage of NC@P/2MZO and NC@P/3MZO is 0.6 mg/mL. Then we fitted the reaction rate constant under the optimal dosage of catalyst. Fig. 6b shows the PFO kinetic curves of the prepared catalysts for TC degradation, as well as the corresponding reaction rate constants (k). NC@P/2MZO had the highest reaction rate constant (0.109 min^{-1}), which was approximately 3.3 times that of pure ZnO. The results in Fig. S17 show that the reaction rate constant of NC@P/2MZO was much higher than those of other reported adsorption-photocatalytic catalysts. This excellent performance was attributed to the good match between the adsorption and photocatalytic rates. After five cycles, the

photocatalytic performance of NC@P/2MZO decreased by less than 10% (Fig. 6c). This slight reduction was attributed to the mass loss of the catalyst and the occupation of the active sites by intermediates. The morphology and lattice structure of the catalyst before and after the reaction did not change significantly (Fig. S18), indicating good stability and practical applicability. To elucidate the mechanism of photocatalytic TC degradation by NC@P/2MZO, active species capture experiments and electron spin resonance spectroscopy (ESR) were used to determine the contributions of various active species to the photocatalytic degradation process. Specifically, P-BQ, IPA, EDTA-2Na, AgNO₃, and carotene were used as trapping agents for $\bullet\text{O}_2^-$, $\bullet\text{OH}$, h^+ , e^- and $^1\text{O}_2$, respectively. After adding these trapping agents to the system, the photocatalytic performance of NC@P/2MZO was evaluated, as shown in Fig. 6d. The photocatalytic performance of NC@P/2MZO was significantly reduced after adding P-BQ, and only 77% of the TC was degraded after 60 min of light irradiation. The photocatalytic properties of NC@P/2MZO also decreased significantly after carotene was added.

We also investigated the effects of various environmental factors on the catalytic performance of NC@P/2MZO, and the results are shown in Fig. S19. For 20 mg/L TC (Fig. S19a), the removal rate reached 87% in darkness for 30 min, and the degradation rate exceeded 90% under light irradiation for 10 min. In contrast, a degradation rate of 90% was only achieved for 100 mg/L TC after irradiation for 60 min. This reduction in catalytic performance was attributed to lower light transmittance because of the higher initial pollutant concentration. When the amount of catalyst increased from 10 to 20 mg (Fig. S19b), the catalytic performance improved significantly. However, further increasing the amount of catalyst also increased the turbidity of the solution. This inhibited light penetration, thereby reducing the absorption of light energy by the catalyst and preventing a significant improvement in degradation efficiency. The effects of the initial pH and anions on the photocatalytic performance of NC@P/2MZO were studied by modulating the pH and the presence of different anions in the aqueous environment. The results presented in Fig. S19c show that acidic conditions were more favorable for TC adsorption. After 40 min of irradiation, NC@P/2MZO degraded TC by more than 90% under all tested initial pH

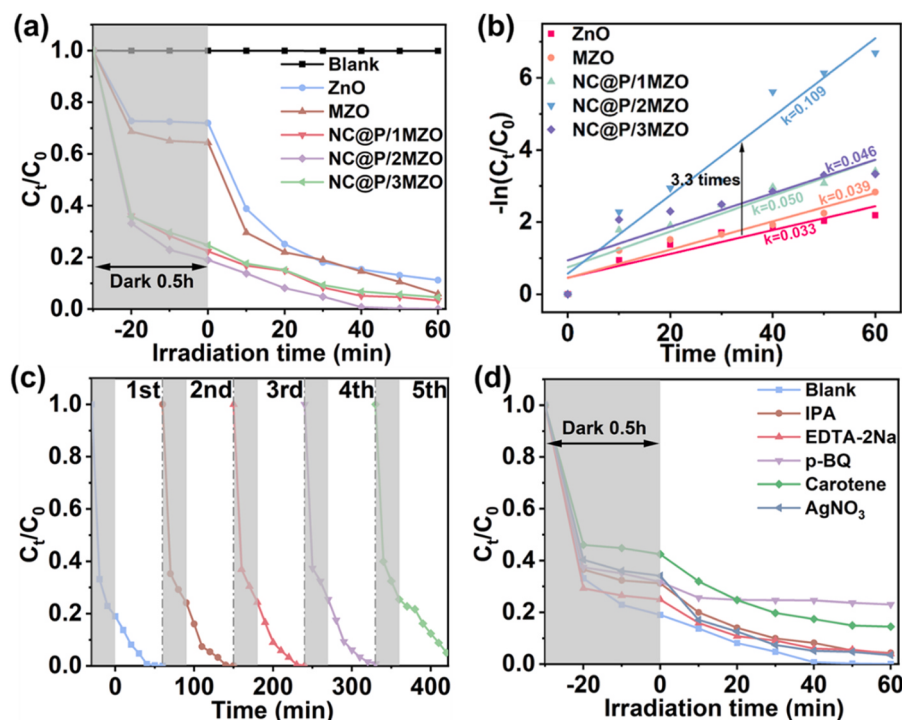


Fig. 6. (a) Photocatalytic TC degradation performance by the prepared catalysts, (b) photocatalytic reaction kinetics of TC degradation with the optimum dosage of catalyst, (c) cyclic tests of photocatalytic performance, (d) photocatalytic degradation curves with various quenchers.

and anion conditions (Fig. S19d), which indicated that NC@P/2MZO has excellent adaptability to natural water environments.

3.5. Degradation pathway and photocatalytic mechanism

LC-MS/MS was employed to analyze the reaction solutions following various irradiation times, and the mass spectra are presented in Fig. S20 [29,53]. Upon increasing the irradiation time, the intensity of the TC peak ($m/z = 445$) decreased gradually, while the intensities of the peaks corresponding to molecules with small m/z values increased gradually; these results indicated that TC was gradually photocatalyzed and decomposed into small molecules and further mineralized by active species. Considering the major intermediates detected, three potential TC photodegradation and transformation mechanisms were proposed (Fig. 7).

Pathway I: First, the methyl group on TC is degraded to form P1 ($m/z = 403$), which is subsequently degraded to P2 ($m/z = 337$) via deamination, deamination, hydroxylation, carbonylation, addition, and ring-opening reactions. Because of the unstable configuration of the enol in P2, this intermediate will be converted into a keto-type structure to form P3, which then loses CH_2O and $\text{C}_2\text{H}_4\text{O}$ to form P4 ($m/z = 297$). These intermediates are further oxidized to low molecular weight organics, such as P9-P15 following functional group dissociation and ring opening.

Pathways II and III: TC is first converted to quinone product P5 (m/z

= 459) and dealkylation product P7 ($m/z = 431$) via oxidation and dealkylation reactions, respectively. Then, P5 is photodegraded to P6 ($m/z = 431$), and P7 is oxidized to carboxylated product P8 ($m/z = 446$). Next, P6 and P8 are transformed into P16 ($m/z = 209$) and P17 ($m/z = 242$) under the action of active oxygen species, respectively. Finally, all of the intermediates are degraded into CO_2 and H_2O , as well as other small molecules.

Fig. 8 shows the ESR spectra of NC@P/2MZO in darkness and light. Characteristic peaks of $\bullet\text{O}_2^-$, $^1\text{O}_2$ and $\bullet\text{OH}$ appeared after 30 s of illumination. In addition, characteristic peaks of h^+ weakened significantly after 30 seconds of illumination. Overall, these results suggest that the main active species in the photocatalytic degradation of TC are $\bullet\text{O}_2^-$, $^1\text{O}_2$, $\bullet\text{OH}$ and h^+ .

ISI-XPS was used to further demonstrate the electron transfer mechanism between NC@PDI and MZO (Fig. 9). After illumination, carbon species migrated to the lower binding energy, indicating that electrons were removed and the surrounding electron cloud density increased. The zinc species migrated to the high binding energy after light exposure, indicating that they lost electrons and the surrounding electron cloud density decreased. In summary, ISI-XPS results confirm that photogenerated electrons transfer from MZO to NC@PDI under light irradiation, providing important evidence for the carrier transfer pathway at the NC@P/MZO heterojunction. More importantly, the migration of photogenerated electrons from MZO to NC@PDI conforms to the S-scheme mechanism.

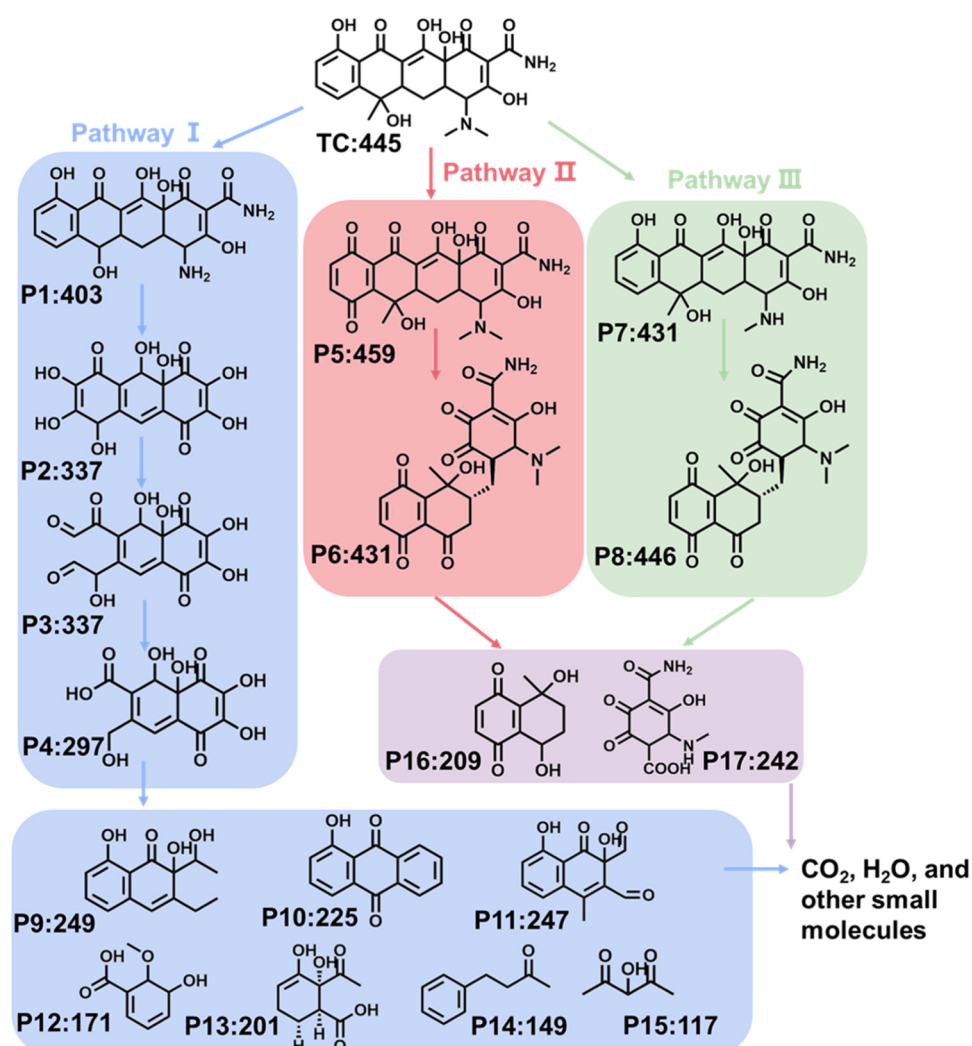


Fig. 7. Proposed pathways of NC@P/2MZO photocatalytic TC degradation.

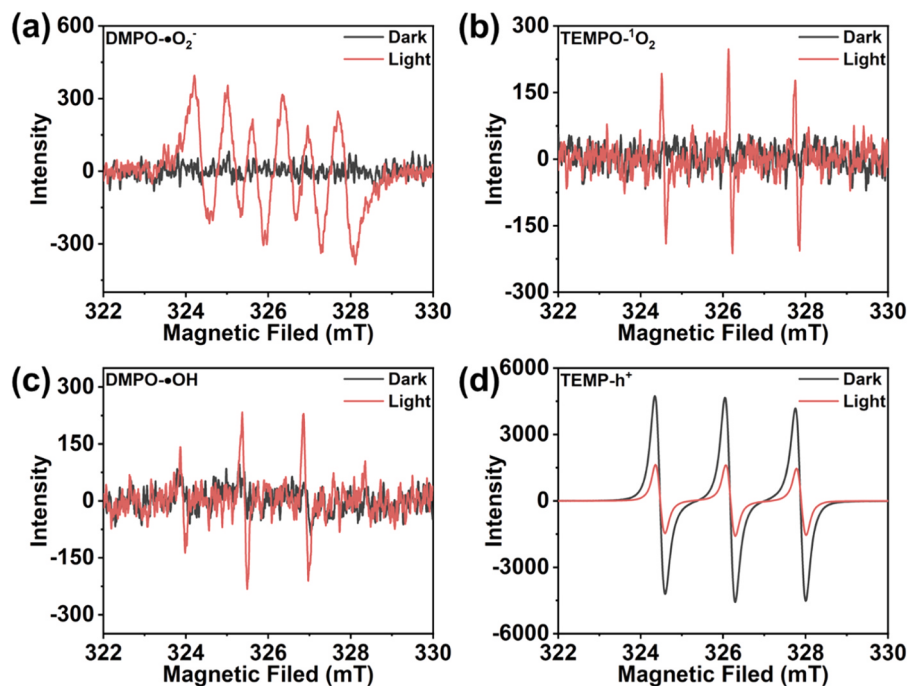


Fig. 8. ESR spectra of (a) DMPO-•O₂⁻, (b) TEMPO-•O₂, (c) DMPO-•OH and (d) DMPO-h⁺ in the dark and under visible light irradiation.

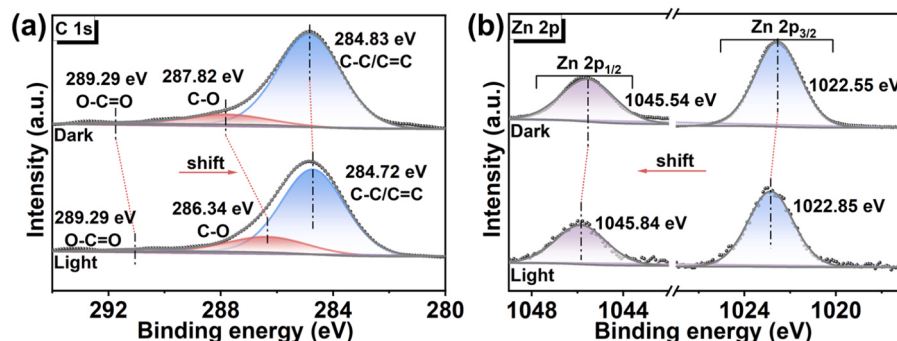
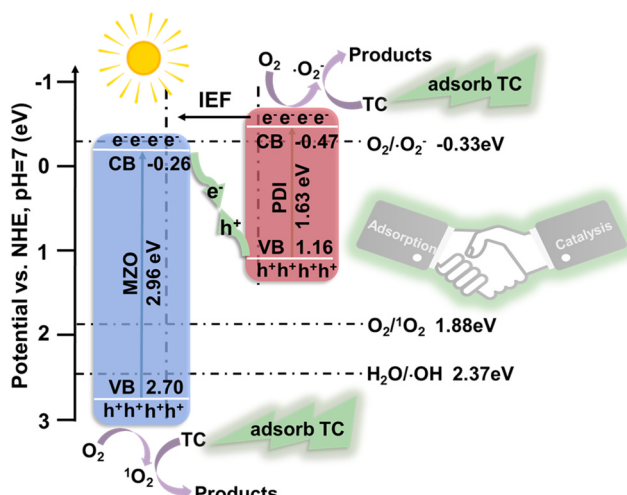


Fig. 9. (a) ISI-XPS high-resolution (a) C 1 s, (b) Zn 2p spectra of NC@P/2MZO in dark and light conditions.

Based on the characterization and photocatalytic experimental results, an S-scheme heterojunction can adequately describe the

synergistic adsorption-photocatalytic TC degradation by NC@P/2MZO (Scheme 2). First, TC molecules in aqueous solution are rapidly adsorbed onto the catalyst surface under dark conditions through pore adsorption, hydrogen bonding, and π - π electron donor-acceptor interactions. According to the ISI-XPS results (Fig. 9), an internal electric field from PDI to MZO is formed at the interface of MZO and PDI. Second, owing to the suitable energy band structure between MZO and PDI, both components generate e^- - h^+ pairs under visible light irradiation. Under the action of the internal electric field, e^- on the conduction band (CB) of MZO are more likely to be transferred to the VB of PDI, thereby accelerating the effective separation of photogenerated carriers. Meanwhile, the strongly oxidizing h^+ on the VB of MZO and the strongly reducing e^- on the CB of PDI continue to accumulate. The e^- on the CB of PDI have a potential of -0.47 eV (vs. NHE), which is more negative than the standard potential of the oxygen reduction reaction, i.e., $O_2/•O_2^-$ (-0.33 eV vs. NHE), and therefore, $•O_2^-$ can be generated. The h^+ potential in the VB of MZO is 2.07 eV, which is higher than the redox potential of oxidizing O_2 to 1O_2 (1.88 eV vs. NHE) [54–56], and therefore, 1O_2 can be generated. Then, $•O_2^-$ and 1O_2 can react directly with TC to further oxidize the TC molecules to produce CO_2 and H_2O , as well as other small molecular products.



Scheme 2. Potential photocatalytic mechanism for TC degradation.

4. Conclusions

Herein, we described the preparation of organic-inorganic hybrid photocatalyst NC@PDI/MZO for TC degradation. The mechanisms governing the adsorption and photocatalysis processes were investigated in detail. The catalyst surface was effectively enriched with TC under the action of pore adsorption, hydrogen bond, and π - π interactions. The NC@P/2MZO catalyst adsorbed 80.0% of 50 mg/L TC after 30 min under dark conditions. Owing to the construction of an S-scheme heterostructure, photogenic carriers could be transferred rapidly, and reactive oxygen species, such as $\bullet\text{O}_2^-$ and $^1\text{O}_2$, were generated. The degradation rate of 20 mg/L TC reached 95.0% after 10 min of irradiation. After 40 min of irradiation, NC@P/2MZO achieved 99.9% degradation of TC (50 mg/L), corresponding to an unprecedented kinetic rate constant of 0.11 min^{-1} . Effective enrichment with TC, enhanced absorption of visible light, and effective separation of photogenerated electron-hole pairs led to a good match of the adsorption and photocatalytic rates, which resulted in ultra-high TC removal performance. This study provides a novel approach for the design and construction of high-performance bifunctional adsorption-photocatalytic catalysts.

CRediT authorship contribution statement

Xu Wanjun: Project administration, Resources, Software. **Chen Dongyun:** Data curation, Funding acquisition, Methodology, Supervision, Writing – review & editing. **Li Najun:** Methodology, Software. **Xu Qingfeng:** Investigation, Methodology, Software. **Li Hua:** Formal analysis, Funding acquisition, Methodology. **Lu Jianmei:** Supervision, Writing – review & editing. **Wang Yaru:** Formal analysis, Methodology, Writing – original draft. **Li Xunxun:** Data curation, Formal analysis, Methodology, Validation, Visualization.

Declaration of Competing Interest

The authors declare that they have no known competing financial interests or personal relationships that could have appeared to influence the work reported in this paper.

Data Availability

Data will be made available on request.

Acknowledgements

We gratefully acknowledge the financial support provided by the National Key Research and Development Program of China (2020YFC1808401, 2020YFC1808403), National Natural Science Foundation of China (22078213, 21938006, 51973148), Basic Research Project of Cutting-Edge Technology in Jiangsu Province (BK20202012), Prospective Application Research Project of Suzhou (SYC2022042), Water Research and Technology Project of Suzhou (2022006), and the Priority Academic Program Development of Jiangsu Higher Education Institutions (PAPD).

Appendix A. Supporting information

Supplementary data associated with this article can be found in the online version at [doi:10.1016/j.apcatb.2024.123839](https://doi.org/10.1016/j.apcatb.2024.123839).

References

- [1] Q. Jin, W. Liu, Y. Dong, Y. Lu, C. Yang, H. Lin, Single atom catalysts for degradation of antibiotics from aqueous environments by advanced oxidation processes: a review, *J. Clean. Prod.* 423 (2023) 138688.
- [2] R. Wang, W. Yu, N. Fang, P. Wang, Y. Chu, S. Wu, J. Liang, Constructing fast charge separation of ZnIn_2S_4 @ CuCo_2S_4 p-n heterojunction for efficient photocatalytic hydrogen energy recovery from quinolone antibiotic wastewater, *Appl. Catal. B Environ.* 341 (2024) 123284.
- [3] W. Xu, X. Zheng, Z. Shangguan, J. Qu, W. Zhang, A low-cost magnetic catalyst (MnFe_2O_4) for ciprofloxacin degradation via periodate activation: The synergistic effect of Mn and Fe, *Chem. Eng. J.* 464 (2023) 142562.
- [4] S. Palsaniya, T. Pal, S. Mukherji, Highly sensitive detection of amoxicillin by polyaniline-AgBr amperometry sensor: Fabrication and application in tap water and lake water, *Chem. Eng. J.* 466 (2023) 143025.
- [5] A. Wang, Z. Zheng, H. Wang, Y. Chen, C. Luo, D. Liang, B. Hu, R. Qiu, K. Yan, 3D hierarchical H₂-reduced Mn-doped CeO₂ microflowers assembled from nanotubes as a high-performance Fenton-like photocatalyst for tetracycline antibiotics degradation, *Appl. Catal. B: Environ.* 277 (2020) 119171.
- [6] W. Zhang, Y. Peng, Y. Yang, L. Zhang, Z. Bian, H. Wang, Bismuth-rich strategy intensifies the molecular oxygen activation and internal electrical field for the photocatalytic degradation of tetracycline hydrochloride, *Chem. Eng. J.* 430 (2022) 132963.
- [7] H. Ren, F. Qi, A. Labidi, J. Zhao, H. Wang, Y. Xin, J. Luo, C. Wang, Chemically bonded carbon quantum dots/Bi₂WO₆ S-scheme heterojunction for boosted photocatalytic antibiotic degradation: Interfacial engineering and mechanism insight, *Appl. Catal. B: Environ.* 330 (2023) 122587.
- [8] X. Wang, J. Zhang, H. Wang, M. Liang, Q. Wang, F. Chen, Revealing the Role of Defect in 3D Graphene-Based Photocatalytic Composite for Efficient Elimination of Antibiotic and Heavy Metal Combined Pollution, *Energy Environ. Mater.*, N./a (2023) e12616.
- [9] X. Wang, Y. Ma, J. Jiang, M. Li, T. Li, C. Li, S. Dong, Cl-based functional group modification MIL-53(Fe) as efficient photocatalysts for degradation of tetracycline hydrochloride, *J. Hazard. Mater.* 434 (2022) 128864.
- [10] X. Wu, X. Wang, I. Lynch, Z. Guo, P. Zhang, L. Wu, Y. Deng, Y. Xie, P. Ning, N. Ren, Strategies to improve photocatalytic activity of nanoscale zero valent iron decorated MoS₂: construction of novel S-scheme nanoflower heterojunction with advanced visible-light degradation of tetracycline, *J. Clean. Prod.* 388 (2023) 135865.
- [11] X. Xu, S. Gong, W. Ji, S. Zhang, Z. Bao, Z. Zhao, Z. Wei, X. Zhong, Z.-T. Hu, J. Wang, Photocatalysis coupling hydrogen peroxide synthesis and in-situ radical transform for tetracycline degradation, *Chem. Eng. J.* 446 (2022) 137009.
- [12] T. Wang, J. Zheng, J. Cai, Q. Liu, X. Zhang, Visible-light-driven photocatalytic degradation of dye and antibiotics by activated biochar composited with K⁺ doped g-C₃N₄: effects, mechanisms, actual wastewater treatment and disinfection, *Sci. Total Environ.* 839 (2022) 155955.
- [13] M. Minale, Z. Gu, A. Guadie, D.M. Kaptamu, Y. Li, X. Wang, Application of graphene-based materials for removal of tetracyclines using adsorption and photocatalytic-degradation: a review, *J. Environ. Manag.* 276 (2020) 111310.
- [14] H. Wang, X. Quan, Q. Xiong, L. Yin, Y. Tian, J. Zhang, Enhanced performance of β -cyclodextrin modified Cu₂O nanocomposite for efficient removal of tetracycline and dyes: synergistic role of adsorption and photocatalysis, *Appl. Surf. Sci.* 621 (2023) 156735.
- [15] X. Song, Y. Wang, T. Zhu, J. Liu, S. Zhang, Facile synthesis a novel core-shell amino functionalized MIL-125(Ti) micro-photocatalyst for enhanced degradation of tetracycline hydrochloride under visible light, *Chem. Eng. J.* 416 (2021) 129126.
- [16] Y. Meng, X. Chen, D. Ai, T. Wei, Z. Fan, B. Wang, Sulfur-doped zero-valent iron supported on biochar for tetracycline adsorption and removal, *J. Clean. Prod.* 379 (2022) 134769.
- [17] G. Yang, Q. Gao, S. Yang, S. Yin, X. Cai, X. Yu, S. Zhang, Y. Fang, Strong adsorption of tetracycline hydrochloride on magnetic carbon-coated cobalt oxide nanoparticles, *Chemosphere* 239 (2020) 124831.
- [18] Q. Shi, W. Wang, H. Zhang, H. Bai, K. Liu, J. Zhang, Z. Li, W. Zhu, Porous biochar derived from walnut shell as an efficient adsorbent for tetracycline removal, *Bioreour. Technol.* 383 (2023) 129213.
- [19] Q. Luo, T. Ren, Z. Lei, Y. Huang, Y. Huang, D. Xu, C. Wan, X. Guo, Y. Wu, Non-toxic chitosan-based hydrogel with strong adsorption and sensitive detection abilities for tetracycline, *Chem. Eng. J.* 427 (2022) 131738.
- [20] H. Xu, Y. Zhang, Y. Wang, L. Zhang, Z. Zhang, L. Zhong, Z. He, Y. Zheng, Y. Shen, Heterojunction material Bi₂YO₃/g-C₃N₄ modified with cellulose nanofibers for photocatalytic degradation of tetracycline, *Carbohydr. Polym.* 312 (2023) 120829.
- [21] Y. Li, B. Yu, Z. Hu, H. Wang, Construction of direct Z-scheme Sn₂@ZnIn₂S₄@kaolinite heterostructure photocatalyst for efficient photocatalytic degradation of tetracycline hydrochloride, *Chem. Eng. J.* 429 (2022) 132105.
- [22] H. Li, H. Ji, J. Liu, W. Liu, F. Li, Z. Shen, Interfacial modulation of ZnIn₂S₄ with high active Cr-S₄ sites for boosting photocatalytic activation of oxygen and degradation of emerging contaminant, *Appl. Catal. B: Environ.* 328 (2023) 122481.
- [23] D. Qiao, Z. Li, J. Duan, X. He, Adsorption and photocatalytic degradation mechanism of magnetic graphene oxide/ZnO nanocomposites for tetracycline contaminants, *Chem. Eng. J.* 400 (2020) 125952.
- [24] Z. Chu, J. Li, H.Y. Sohn, C. Chen, X. Huang, Y. Lan, A. Murali, J. Zhang, CeO₂-g-C₃N₄ S-scheme heterojunctions for enhanced photocatalytic performance: effects of surface C/N ratio on photocatalytic and adsorption properties, *Compos., Part B* 257 (2023) 110689.
- [25] C. Tian, H. Zhao, H. Sun, K. Xiao, P. Keung, Wong, Enhanced adsorption and photocatalytic activities of ultrathin graphitic carbon nitride nanosheets: Kinetics and mechanism, *Chem. Eng. J.* 381 (2020) 122760.
- [26] X. Zou, L. Yao, S. Zhou, G. Chen, S. Wang, X. Liu, Y. Jiang, Sulfated lignocellulose nanofibril based composite aerogel towards adsorption-photocatalytic removal of tetracycline, *Carbohydr. Polym.* 296 (2022) 119970.

[27] C. Du, S. He, Y. Xing, Q. Zhao, C. Yu, X. Su, J. Feng, J. Sun, S. Dong, Fabricating S-scheme $\text{BiOBr}/\text{Zn}_2\text{In}_2\text{S}_3$ heterojunction for synergistic adsorption-photocatalytic degradation of tetracycline, *Mater. Today Phys.* 27 (2022) 100827.

[28] Y. Zhou, T. Cai, S. Liu, Y. Liu, H. Chen, Z. Li, J. Du, Z. Lei, H. Peng, N-doped magnetic three-dimensional carbon microspheres@ TiO_2 with a porous architecture for enhanced degradation of tetracycline and methyl orange via adsorption/photocatalysis synergy, *Chem. Eng. J.* 411 (2021) 128615.

[29] Z. He, M.S. Siddique, H. Yang, Y. Xia, J. Su, B. Tang, L. Wang, L. Kang, Z. Huang, Novel Z-scheme $\text{In}_2\text{S}_3/\text{Bi}_2\text{WO}_6$ core-shell heterojunctions with synergistic enhanced photocatalytic degradation of tetracycline hydrochloride, *J. Clean. Prod.* 339 (2022) 130634.

[30] S. Wang, Y. Xia, G. Yan, M. Chen, X. Wang, L. Wu, R. Liang, PDI bridged MIL-125 (Ti)-NH₂ heterojunction with frustrated Lewis pairs: a promising photocatalyst for Cr(VI) reduction and antibacterial application, *Appl. Catal. B: Environ.* 317 (2022) 121798.

[31] M. Wang, Y. Zhang, D. Chen, N. Li, Q. Xu, H. Li, J. Lu, Biomimetic porphyrin-modified 3D porous composite material adsorption enhances photocatalytic CO_2 reduction and tetracycline oxidative degradation, *Chem. Eng. J.* 469 (2023) 144064.

[32] W. Li, H. Zhang, S. Huang, J. Xu, L. Liu, J. Li, J. Jing, Y. Zhu, Electron-enriched supramolecular PDI- SiO_2 promoting PDS activation for enhanced photocatalytic advanced oxidation, *Appl. Catal. B: Environ.* 340 (2024) 123262.

[33] Y. Guo, B. Liu, J. Zhang, G. Wang, C. Pan, H. Zhao, C. Wang, F. Yu, Y. Dong, Y. Zhu, Perylene imide supermolecule promote oxygen to superoxide radical for ultrafast photo-oxidation of 5-hydroxymethylfurfural, *Appl. Catal. B: Environ.* 340 (2024) 123217.

[34] X. Li, Y. Wang, D. Chen, N. Li, Q. Xu, H. Li, J. He, J. Lu, A highly dispersed Pt/copper modified- MnO_2 catalyst for the complete oxidation of volatile organic compounds: The effect of oxygen species on the catalytic mechanism, *Green. Energy Environ.* 8 (2023) 538–547.

[35] Y. Wang, X. Li, J. He, J. Xiao, D. Chen, N. Li, Q. Xu, H. Li, J. Lu, Manganese dioxide supported on hollow graphitized carbon spheres for the catalytic oxidation of toluene: Improved adsorption and electron transfer, *Sep. Purif. Technol.* 321 (2023) 124203.

[36] M. Wang, D. Chen, N. Li, Q. Xu, H. Li, J. He, J. Lu, Ni-Co Bimetallic Hydroxide Nanosheet Arrays Anchored on Graphene for Adsorption-Induced Enhanced Photocatalytic CO_2 Reduction, *Adv. Mater.* 34 (2022) 2202960.

[37] Y. Luo, J. Xu, P. Mou, L. Li, Y. Chen, L. Yan, H. Yu, J. Shu, L. Zhang, Cobalt/Nitrogen Co-Doped carbon materials enhance the reaction rate of sodium-potassium alloy electrodes, *Small*, N./a (2023) 2304981.

[38] Z. Zhou, S. Pourhashem, Z. Wang, J. Duan, R. Zhang, B. Hou, Distinctive roles of graphene oxide, ZnO quantum dots, and their nanohybrids in anti-corrosion and anti-fouling performance of waterborne epoxy coatings, *Chem. Eng. J.* 439 (2022) 135765.

[39] Y. Wang, X. Li, J. Xiao, D. Chen, N. Li, Q. Xu, H. Li, J. He, J. Lu, Metal-organic frameworks-derived manganese trioxide with uniformly loaded ultrasmall platinum nanoparticles boosting benzene combustion, *Sci. Total Environ.* 839 (2022) 156345.

[40] R. Gang, L. Xu, Y. Xia, J. Cai, L. Zhang, S. Wang, R. Li, Fabrication of MoS_2 QDs/ ZnO nanosheet 0D/2D heterojunction photocatalysts for organic dyes and gaseous heavy metal removal, *J. Colloid Interface Sci.* 579 (2020) 853–861.

[41] G. Zhang, D. Chen, N. Li, Q. Xu, H. Li, J. He, J. Lu, Construction of Hierarchical Hollow $\text{Co}_9\text{S}_8/\text{ZnIn}_2\text{S}_4$ tubular heterostructures for highly efficient solar energy conversion and environmental remediation, *Angew. Chem., Int. Ed.* 59 (2020) 8255–8261.

[42] G. Zhang, X. Li, D. Chen, N. Li, Q. Xu, H. Li, J. Lu, Internal Electric Field and Adsorption Effect synergistically boost carbon dioxide conversion on cadmium sulfide@covalent triazine frameworks core-shell photocatalyst, *Adv. Funct. Mater.*, N./a (2023) 2308553.

[43] G. Zhang, D. Chen, N. Li, Q. Xu, H. Li, J. He, J. Lu, Fabrication of $\text{Bi}_2\text{MoO}_6/\text{ZnO}$ hierarchical heterostructures with enhanced visible-light photocatalytic activity, *Appl. Catal. B: Environ.* 250 (2019) 313–324.

[44] X. Jia, C. Hu, H. Sun, J. Cao, H. Lin, X. Li, S. Chen, A dual defect co-modified S-scheme heterojunction for boosting photocatalytic CO_2 reduction coupled with tetracycline oxidation, *Appl. Catal. B: Environ.* 324 (2023) 122232.

[45] G. Wang, H. Li, N. Li, D. Chen, J. He, Q. Xu, J. Lu, Construction of Perylene-based Amphiphilic micelle and its efficient adsorption and in situ photodegradation of bisphenol A in aqueous solution, *Angew. Chem., Int. Ed.* 61 (2022) e202210619.

[46] H. Deng, A. Li, C. Ye, L. Sheng, Z. Li, Y. Jiang, Green removal of various pollutants by microsphere adsorption: material characterization and adsorption behavior, *Energy Fuels* 34 (2020) 16330–16340.

[47] D. Wang, F. Jia, H. Wang, F. Chen, Y. Fang, W. Dong, G. Zeng, X. Li, Q. Yang, X. Yuan, Simultaneously efficient adsorption and photocatalytic degradation of tetracycline by Fe-based MOFs, *J. Colloid Interface Sci.* 519 (2018) 273–284.

[48] M. Wei, F. Marrakchi, C. Yuan, X. Cheng, D. Jiang, F.F. Zafar, Y. Fu, S. Wang, Adsorption modeling, thermodynamics, and DFT simulation of tetracycline onto mesoporous and high-surface-area NaOH-activated macroalgae carbon, *J. Hazard. Mater.* 425 (2022) 127887.

[49] W. Zhang, Z. Bian, Y. Peng, H. Tang, H. Wang, Dual-function oxygen vacancy of BiOBr intensifies pollutant adsorption and molecular oxygen activation to remove tetracycline hydrochloride, *Chem. Eng. J.* 451 (2023) 13873.

[50] R. Herazo, M. Mueses, G. Li Pumac, F. Martínez, Impact of photocatalyst optical properties on the efficiency of solar photocatalytic reactors rationalized by the concepts of initial rate of photon absorption (IRPA) dimensionless boundary layer of photon absorption and apparent optical thickness, *Chem. Eng. J.* 356 (2019) 839–849.

[51] I. Grcica, N. Koprivanac, G. Li, Puma, Modeling the photocatalytic oxidation of carboxylic acids on aqueous TiO_2 suspensions and on immobilized TiO_2 -chitosan thin films in different reactor geometries irradiated by UVA or UVC light sources, *Chem. Eng. J.* 422 (2021) 130104.

[52] M. Misrac, S. Chowdhury, T. Leeb, Sunlight driven decomposition of toxic organic compound, coumarin, p-nitrophenol, and photo reduction of Cr(VI) ions, using a bridge structure of Au@CNT@ TiO_2 nanocomposite, *Appl. Catal. B: Environ.* 272 (2020) 118991.

[53] H. Jiang, Q. Wang, P. Chen, H. Zheng, J. Shi, H. Shu, Y. Liu, Photocatalytic degradation of tetracycline by using a regenerable (Bi)BiOBr/rGO composite, *J. Clean. Prod.* 339 (2022) 130771.

[54] J. Zheng, C. Fan, X. Li, Q. Yang, D. Wang, A. Duan, J. Ding, S. Rong, Z. Chen, J. Luo, B. Zhang, Enhanced photodegradation of tetracycline hydrochloride by hexameric AgBr/Zn-Al MMO S-scheme heterojunction photocatalysts: Low metal leaching, degradation mechanism and intermediates, *Chem. Eng. J.* 446 (2022) 137371.

[55] K. Dou, C. Peng, R. Wang, H. Cao, C. Yao, J. Qiu, J. Liu, N. Tsidaeva, W. Wang, S-scheme tubular $\text{g-C}_3\text{N}_4/\text{BiOI}$ heterojunctions for boosting photodegradation of tetracycline and Cr(VI): mechanism insight, degradation pathway and DFT calculation, *Chem. Eng. J.* 455 (2023) 140813.

[56] S. Li, C. Wang, Y. Liu, M. Cai, Y. Wang, H. Zhang, Y. Guo, W. Zhao, Z. Wang, X. Chen, Photocatalytic degradation of tetracycline antibiotic by a novel $\text{Bi}_2\text{Sn}_2\text{O}_7/\text{Bi}_2\text{MoO}_6$ S-scheme heterojunction: performance, mechanism insight and toxicity assessment, *Chem. Eng. J.* 429 (2022) 132519.